Cellular co-infection increases the speed and efficiency of influenza A virus production and shapes the interferon response to infection

Brigitte E. Martin[1]*, Jeremy D. Harris[3]*, Jiayi Sun[1], Katia Koelle[3], Christopher B. Brooke[1,2]

[1] Department of Microbiology, University of Illinois at Urbana-Champaign, Urbana, IL
[2] Carl R. Woese Institute for Genomic Biology, University of Illinois at Urbana-Champaign, Urbana, IL
[3] Department of Biology, Emory University, Atlanta, GA
* Authors contributed equally

Corresponding authors: Christopher Brooke (cbrooke@illinois.edu) and Katia Koelle (katia.koelle@emory.edu)

ABSTRACT

During viral infection, the numbers of virions infecting individual cells can vary significantly over time and space. The functional consequences of this variation in cellular multiplicity of infection (MOI) remain poorly understood. Here, we rigorously quantify the phenotypic consequences of cellular MOI during influenza A virus (IAV) infection over a single round of replication in terms of cell death rates, viral output kinetics, interferon production, and superinfection potential. By statistically fitting mathematical models to our data, we precisely define the specific functional forms that govern the modulation of these phenotypes by MOI at the single cell level. We find that cellular co-infection increases the rate and efficiency of virus production, suggesting a potential role for co-infection in influencing viral fitness. We also find that infected cell death rates and type I interferon expression are independent of viral input while type III interferon induction is highly dependent on cellular MOI, identifying a role for cellular co-infection in shaping the host immune response to IAV infection. Finally, we show that increasing viral input is associated with more potent superinfection exclusion, thus limiting the total number of virions capable of infecting a cell. Overall, this study suggests that the extent of cellular co-infection by influenza viruses may be a critical determinant of both viral fitness and infection outcome.

AUTHOR SUMMARY

During influenza A virus (IAV) infection the number of virions to enter individual cells can be highly variable. Cellular co-infection appears to be common and plays an essential role in facilitating reassortment for IAV, yet little is known about how cellular co-infection influences infection outcomes at the cellular level. Here, we combine quantitative *in vitro* infection experiments with statistical model fitting to precisely define the phenotypic consequences of cellular co-infection. We reveal that cellular co-infection both accelerates and increases the efficiency of IAV production, identifying it as a potential determinant of viral fitness. We also show that induction of type III, but not type I, interferon is highly dependent upon the number of virions that infect a given cell, implicating cellular co-infection as an unappreciated determinant of the host innate immune response to infection. Altogether, our findings show that cellular co-infection plays a crucial role in determining infection outcome. The integration of experimental and statistical modeling approaches detailed here represents a significant advance in the quantitative study of influenza virus infection and should aid ongoing efforts focused on the construction of mathematical models of IAV infection.

INTRODUCTION

Cellular co-infection plays an important, yet poorly defined role in shaping the outcome of influenza A virus (IAV) infection. By facilitating reassortment between incoming viral genomes, cellular co-infection can give rise to new viral genotypes with increased fitness or emergence potential (1). Cellular co-infection can also enhance the replicative potential of the virus by promoting the complementation and multiplicity reactivation of the semi-infectious particles that constitute the bulk of influenza virus populations (2–4). Despite its clear importance, the prevalence and the specific functional consequences of cellular co-infection during IAV infection remain largely unknown.

We and others have previously shown that cellular co-infection can be common *in vivo* (5,6). There is growing evidence that IAV replication and spread is focal and thus that the distribution of individual virions across cells and tissues is highly spatially structured, resulting in foci of high cellular multiplicity of infection (MOI) (7–10). Given the dynamic distribution of virions over time and space during infection, it appears likely that the MOIs of individual infected cells can vary significantly. This raises the question whether this variation in the number of virions that infect a cell has distinct phenotypic consequences. If so, it could have significant implications for understanding IAV infection dynamics as two viral populations of identical size and genome sequence could give rise to divergent infection outcomes if the dispersal patterns of virions (and thus the MOI distribution across cells) differs.

Several previous studies have suggested that the number of virions that enter a given cell (referred to throughout as “cellular MOI” or “viral input”) may affect replication kinetics and interferon (IFN) induction (11–14); however, the phenotypic consequences of cellular MOI during IAV infection have not yet been rigorously or comprehensively quantified. Here, we combine precise single-cycle infection experiments with statistical model fitting to reveal that cellular MOI significantly alters virus production rates, the host response to infection, and the potential for further superinfection. In doing so, we precisely define the functional forms that govern the relationships between the amount of viral input and the phenotypes of infected cells, information that will aid future efforts to quantitatively model IAV infection. Altogether, these results reveal and define an unappreciated role for cellular co-infection in shaping the outcome of IAV infection.

RESULTS

To define how variation in cellular MOI affects viral replication dynamics and the host response to infection, we infected either MDCK or A549 cells with A/Puerto Rico/8/1934 (PR8) across a 100-fold range of MOIs. To eliminate the confounding effects of secondary spread within culture on MOI and replication kinetics, we limited infections to a single cycle by treating cells with 25 mM NH4Cl at 2 hpi (15). Thus, in all experiments described below, we were examining the outcome of a single round of infection.

Precise quantification of the actual MOI

An accurate definition of the phenotypic consequences of cellular co-infection depends upon the precise measurement of the average number of viral genomes that actually contribute to infection. We suspected that the standard method for calculating bulk MOI, based on the dilutions of viral working stock used, may overestimate the actual mean number of virions that successfully infect.

To calculate the “actual” bulk MOI (referred to hereafter as “bulk MOI”), we quantified the fraction of virus added to cells that was successfully bound or taken up during the adsorption phase. We

first measured the concentration of virus present in the inoculum added to cells (0 hpi) and the amount of remaining unbound virus following 1 hour adsorption at 4ºC (1 hpi) across a range of bulk MOIs by RT-qPCR (**Fig. S1**). Cells were washed extensively and transitioned to growth media following the 1 hr adsorption period. To confirm that our post-adsorption washes effectively removed any unbound inoculum virus that could artificially inflate subsequent viral output measurements, we quantified extracellular virus immediately following wash and found that viral loads were negligible (<10^3 genome equivalent (GE)/mL; data not shown). At 2 hours post-adsorption (3 hpi), we again measured the amount of extracellular virus present and found titers that were surprisingly high for this early timepoint, especially at an intended bulk MOI of 10 (**Fig. S1**).

To determine whether extracellular virus present at 3 hpi represented new virus production, we repeated the above experiments in the presence of 40 μM of the antiviral drug T-705, which inhibits the production of viral progeny (16). Drug treatment significantly reduced viral titers at 6 hpi, but not 3 hpi, indicating that extracellular virus measured at 3 hpi represented inoculum virus that was taken up but then released without actually infecting the cell (**Fig. 1A**). Thus, to precisely quantify the actual bulk MOI of virus that contributed to infection, we subtracted extracellular virus detected at both 1 hpi and 3 hpi from our original estimates of bulk MOI. This gave us an actual bulk MOI range of 0.23-7.32 (**Fig. 1B**).

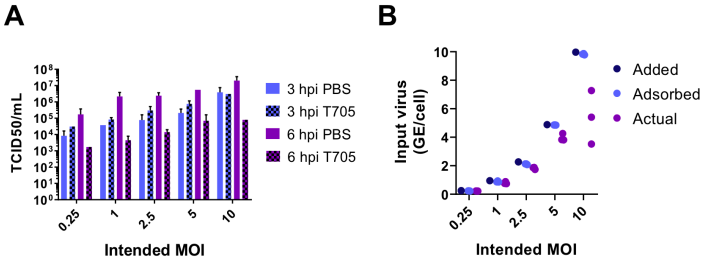

Fig. 1. Precise quantification of actual MOI. (A) Effect of 40 uM T705 treatment on extracellular virus titers at 3 hpi and 6 hpi. MDCK cells were infected with PR8 at the indicated MOIs in the absence (PBS; solid bars) or presence of T705 (checkered bars). TCID50 present in supernatant was measured at 3 hpi and 6 hpi. **(B)** Quantification by RT-qPCR of virus present in inoculum (0 hpi; "added MOI"), virus adsorbed to cells after 1 hpi (calculated by subtracting extracellular virus present at 1hpi from that present in input at 0 hpi; "adsorbed MOI"), and virus expected to actually contribute to infection (calculated by subtracting 1hpi and 3hpi GE amounts from input 0 hpi amount; "actual MOI") for each of the indicated intended bulk MOI groups. Data presented as viral genome equivalents (GE) per cell, with each point showing data from a single infection well.

Cell death rates are time-dependent but virus input-independent

The productivity of an infected cell depends in part upon how long the cell lives following infection, and we suspected that cellular lifespans might be affected by cellular MOI. Once we could precisely measure the actual bulk MOI for different infection groups, we quantified how changes in bulk MOI affected cell loss following infection using trypan blue exclusion. As expected, the percentage of surviving cells generally decreased with higher bulk MOIs for each timepoint tested (**Fig. 2A-D**). To determine whether the observed decrease in the percentage of surviving cells was simply the effect of increasing the number of infected cells, or whether cells co-infected with multiple virions died at a faster rate than singly-infected cells, we statistically fit a set of mathematical models to the experimental data (Methods).

We first considered a model in which all infected cells died at a constant rate over the course of infection. However, this model systematically overestimated the percentage of surviving cells at early time points following infection (3 and 6 hpi; **Figs. 2A,B**) and systematically underestimated the percentage of surviving cells at the latest time point (18 hpi; **Fig. 2D**). We next considered a model in which cell death rates were able to change over the course of infection. This model still assumed that infected cell death rates were independent of cellular MOI. Fitting of this model to the data yielded an infected cell death rate that decreased over time (**Fig. 2E, Table 1**). At all time points examined, this model quantitatively reproduced the experimental data (**Fig. 2A-D**), and a statistical comparison between the two models indicated that the time-dependent cell death rate model is strongly preferred over the time-independent death rate model (ΔAIC = 37.5, **Table 1**). The ability of the time-dependent death rate model to reproduce the data indicates that death rate differences arising from differences in cellular MOI do not need to be invoked to explain the observed experimental data. Indeed, an alternative model that assumed that death rates are time-independent, but scale linearly with cellular MOI, performed worse than the simplest model with death rates that are independent of both time and cellular input (**Fig 2A-D, Table 1**). These findings suggest that once a cell is infected, the kinetics of cell death are unaffected by increasing cellular MOI.

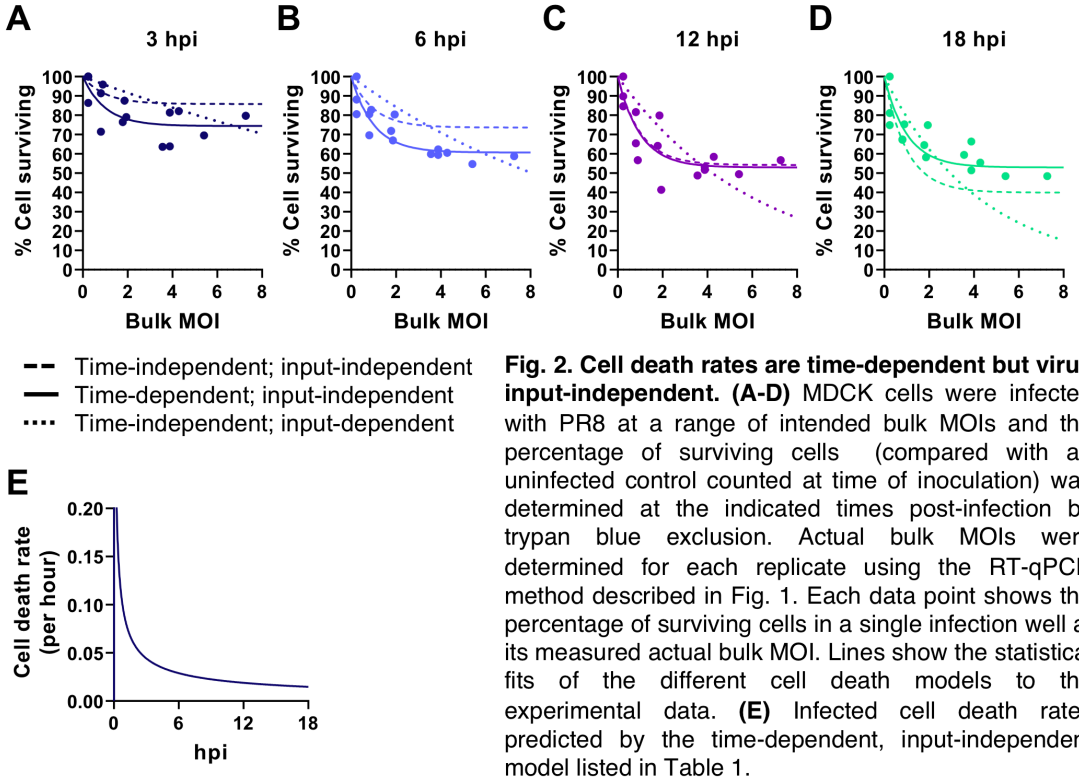

Fig. 2. Cell death rates are time-dependent but virus input-independent. (A-D) MDCK cells were infected with PR8 at a range of intended bulk MOIs and the percentage of surviving cells (compared with an uninfected control counted at time of inoculation) was determined at the indicated times post-infection by trypan blue exclusion. Actual bulk MOIs were determined for each replicate using the RT-qPCR method described in Fig. 1. Each data point shows the percentage of surviving cells in a single infection well at its measured actual bulk MOI. Lines show the statistical fits of the different cell death models to the experimental data. **(E)** Infected cell death rates predicted by the time-dependent, input-independent model listed in Table 1.

Table 1. Death rate models and their fit to data.

Model	Death rate function	Parameter estimates	RSS	ΔAIC	Parameter legend
Time-independent, input-independent death rate	$\alpha(t,i) = a$	$a = 0.051$	0.845	37.5	a = constant death rate (per hour)
Time-dependent, input-independent death rate	$\alpha(t,i) = b\,k\,t^{k-1}$	$b = 0.224$, $k = 0.387$	0.437	0	b = scale parameter, k = shape parameter
Time-independent, input-dependent death rate	$\alpha(t,i) = c\,i$	$c = 0.015$	1.262	63.6	c = per capita death rate (per hour, per virus particle)

Table 1. Death rate models and their fit to data. Rows show the three considered models. For each model, the table lists the functional form of the death rate that the model assumes (α), with t represents time since infection (hpi) and i represents cellular input. The table also lists model parameter estimates, the residual sum of squares (RSS) of the parameterized model, and calculated ΔAIC values. ΔAIC values are calculated by taking the difference between a given model and the model with the lowest AIC value, with AIC values of a model calculated using the equation $2k + n \ln(\text{RSS})$, where k is the number of estimated parameters and n is the number of data points ($n = 60$).

149
150
151 **Cellular co-infection increases the rate of virus production**
152 We next asked how changes in bulk MOI affected virus production over a single cycle of infection.
153 In the same experiments described above, we measured the total viral output (in GE/mL) from
154 cells infected at different bulk MOIs at 6, 12, and 18 hpi. Not surprisingly, we observed that viral
155 output was significantly higher at higher bulk MOIs for all time points tested (**Fig. 3A**). This effect
156 was more pronounced at 6 hpi compared with 12 hpi or 18 hpi ($p = 0.0024$ and 0.0002 respectively,
157 by one-way ANOVA Tukey's multiple comparison test).
158

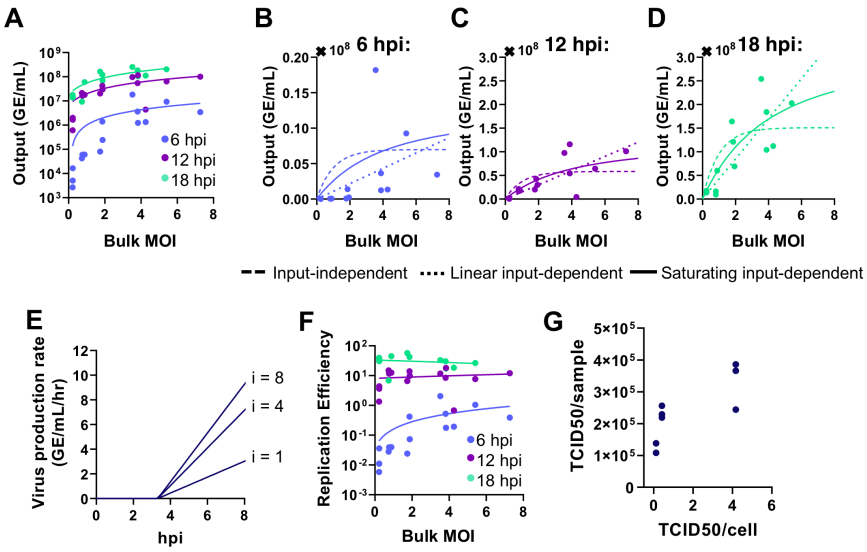

Fig. 3. Cellular co-infection increases the rate and efficiency of virus production. (A) Virus output from MDCK cells infected with PR8 over the indicated range of bulk MOIs. The total viral output (GE/mL) from single cycle infections was measured by RT-qPCR at the indicated times post-infection and plotted as a function of the bulk MOI for each infection well. Trend lines represent linear regressions (log(GE/mL), log(MOI) scale) for each timepoint (6 hpi: slope (m) = 2.15, R^2 = 0.87, slope significantly non-zero: $p < 0.0001$; 12 hpi: slope (m) = 1.13, R^2 = 0.69, slope significantly non-zero: $p = 0.0001$; 18 hpi slope (m) = 0.90, R^2 = 0.76, slope significantly non-zero: $p < 0.0001$) plotted on the semilog scale. One-way ANOVA Tukey's multiple comparison of effects of MOI on viral output at 6 hpi vs 12 hpi ($p = 0.0024$) or 18 hpi ($p = 0.0002$). **(B-D)** Different time-dependent virus output models statistically fit to viral output data at the indicated timepoints. **(E)** Model-predicted virus output dynamics. Predictions are shown for the best virus output model, as determined by ΔAIC (the time-dependent, saturating input-dependent model). Dynamics for various cellular input levels (i = 1, 4, 8) are shown as a function of time. **(F)** Viral replication efficiency (calculated as the ratio of output viral genomes over mean input viral genomes) plotted at each timepoint as a function of bulk MOI. Trend lines represent linear regressions (on the log(replication efficiency), log(MOI) scale) for data from each timepoint, plotted on the semilog scale. At 12 hpi and 18 hpi, the proportion of replication efficiency variance that was explained by MOI was small (R^2 = 0.08 and R^2 = 0.004, respectively). At 6 hpi, the proportion of replication efficiency variance that was explained by MOI was greater (R^2 = 0.71) and the correlation between MOI and virus output was significantly positive ($p < 0.0001$). **(G)** 2.5×10^6 TCID50 of PR8 virions were used to infect differing numbers of MDCK cells (6×10^5, 6×10^6, and 2×10^7), and viral output per sample was quantified by TCID50 at 6 hpi. Data are presented as total output TCID50 per sample.

These findings raised the question of whether the increase in viral output at higher bulk MOIs is simply a function of increases in the number of infected cells, or whether individual infected cells produce more virus output when co-infected by multiple virions. To precisely define the functional relationship between cellular MOI and viral output, we again statistically fit several mathematical models to our data (Methods). The first three models we fit were all time-independent and thus assumed that the rate of virus output did not change over the course of infection. These three models differed in their assumed relationship between virus input and virus output: the first assumed that all infected cells produce progeny virus at equal rates (no matter how many input genomes enter a cell; input-independent), the second model assumed that the rate of virus output scales linearly with the number of genomes that enter a cell (linear input-dependent), and the third model assumed that the rate of virus output increases with the number of genomes that enter a cell, but with saturation of virus output at high virus input (saturating input-dependent). **Table 2** shows the statistical fits of these time-independent models to the data shown in Fig. 3A. All three models overestimated virus output at 6 hpi and underestimated virus output at 18 hpi, across all bulk MOIs examined (**Fig. S2**).

Table 2. Virus output models and their fit to data.

Model (time-independent)	Production rate function	Parameter estimates	RSS	ΔAIC	Parameter legend
Input-independent	$\nu(t,i) = l$	$l = 5.169$	7.58E+16	29.5	l = constant production rate (per hour)
Linear input-dependent	$\nu(t,i) = r\,i$	$r = 1.331$	8.13E+16	32.6	r = slope of per virion production rate (per hour, per virus particle)
Saturating input-dependent	$\nu(t,i) = \frac{m\,i}{(K+i)}$	$m = 8.932$, $K = 1.974$	6.86E+16	27.1	m = max production rate (per hour), K = input at half max rate
Model (time-dependent)	**production rate function**	**Parameter estimates**	**RSS**	**ΔAIC**	**Parameter legend**
Input-independent	$\nu(t,i) = \begin{cases} l\,(t-s) & , \; t > s \\ 0 & , \; \text{otherwise} \end{cases}$	$l = 1.229$ $s = 3.068$	4.67E+16	10.3	l = slope of linear production rate (per hour), s = hpi at which production begins
Linear input-dependent	$\nu(t,i) = \begin{cases} r\,(t-s)\,i & , \; t > s \\ 0 & , \; \text{otherwise} \end{cases}$	$r = 0.393$ $s = 3.950$	4.17E+16	5.3	r = slope of per virion linear production rate (per hour, per virus particle) s = hpi at which production begins
Saturating input-dependent	$\nu(t,i) = \begin{cases} \frac{m\,(t-s)\,i}{(K+i)} & , \; t > s \\ 0 & , \; \text{otherwise} \end{cases}$	$m = 2.808$ $K = 3.350$ $s = 3.314$	3.53E+16	0	m = max production rate (per hour), K = input at half max rate, s = hpi at which production begins

Table 2. Virus output models and their fit to data. Rows show the three time-independent models and the three time-dependent models considered. For each model, the table lists the functional form for the virus production rate ν, with t representing time since infection (hpi) and i representing cellular input. The table also lists model parameter estimates, the residual sum of squares (RSS) of the parameterized model, and calculated ΔAIC values. For the calculations of ΔAIC, the number of data points is $n = 40$

Thus, we considered three additional models that allowed virus output to change over the course of infection (time-dependent). As before, these three models differed from one another with respect to their assumptions of how virus input impacted virus output (input-independent, linear input-dependent, and saturating input-dependent). All three of these time-dependent models performed better than the three time-independent models; however, the third time-dependent model significantly outperformed both other time-dependent models (**Fig 3B-D; Table 2**). **Fig. 3E** shows estimated rates of virus production over time and for several illustrative virus inputs for this preferred model. These results indicate that virus output begins 3-4 hours post-infection, followed by an increasing rate of virus production that is, up to a point, higher in cells infected by more virions. These results are consistent with previous reports of earlier and higher rates of replication under high experimental MOI conditions (17,18).

Increased cellular co-infection enhances the efficiency of viral replication

To control for the differences in input genomes across the different bulk MOI conditions, we calculated the efficiency of infection by dividing the number of output viral genomes by the number of input genomes (**Fig. 3F**). Increasing the bulk MOI significantly increased the efficiency of infection at 6 hpi ($R^2 = 0.71$, $p < 0.0001$); however, a positive correlation between bulk MOI and infection efficiency was no longer apparent at later timepoints (12 hpi $p = 0.31$; 18 hpi $p = 0.82$). This is likely due to a combination of virus production rates saturating at high cellular MOIs and increases in virus production rates over the course of infection. Importantly, cells infected at higher

196 bulk MOI crossed the threshold into positive virus production (virus output/input > 1) by 6 hpi,
197 while the lower MOI infections lagged. These results suggest that increasing the number of virions
198 introduced into a given cell increases the efficiency of viral progeny production.
199
200 To further confirm this effect, we performed single cycle infection experiments in which we added
201 a constant virus population size (2.5×10^6 TCID50) to three different population sizes of target
202 MDCK cells: 6×10^5, 6×10^6, and 2×10^7. This approach allowed us to vary the bulk MOI while
203 maintaining a constant viral population size, thus mimicking the effects of varying the degree of
204 spatial diffusion of virions across a tissue surface. At 6 hpi we observed a modest but statistically
205 significant increase in viral output as bulk MOI increases ($p=0.0041$ by one-way ANOVA on effect
206 of MOI), further supporting the conclusion that increasing the extent of cellular co-infection
207 increases the efficiency of viral replication (**Fig. 3G**). Importantly, this result suggests that the
208 spatial distribution of virions may serve as an important determinant of viral replicative potential,
209 consistent with a recent analysis of the effects of spatial structure on IAV replication (19).
210
211 **Cellular co-infection enhances type III (but not type I) IFN induction**
212 In addition to affecting virus production, cellular MOI also has the potential to affect the activation
213 of innate immunity. A prior study observed that the magnitude of interferon (IFN) transcription
214 during IAV infection is higher under higher experimental MOI conditions (11); however, this
215 relationship was not rigorously defined and it was not clear whether this effect simply arose from
216 increases in infected cell numbers. A more recent study suggests that increasing cellular MOI
217 might actually result in more potent antagonism of IFN activation (14). To precisely define the
218 effects of cellular co-infection on innate immune activation, we measured the effects of varying
219 bulk MOI on the induction of both type I (IFNB1) and type III (IFNL1) IFN transcription in A549
220 cells at 8 and 18 hpi within a single cycle of viral replication.
221
222 Surprisingly, we observed that IFNB1 and IFNL1 expression responded very differently to
223 increasing bulk MOI. By 8 hpi, IFNB1 expression was significantly elevated above mock under all
224 MOI conditions (**Fig. 4A**); we did not find a positive correlation between bulk MOI and levels of
225 IFNB1 induction ($p = 0.78$). This suggests that IFNB1 induction (at least in bulk) is independent
226 of MOI or even the total number of infected cells in the culture. By 18 hpi, we did observe a
227 statistically significant positive correlation between bulk MOI and IFNB1 induction ($p = 0.0002$);
228 however, this effect was quite small (slope = 0.17).
229

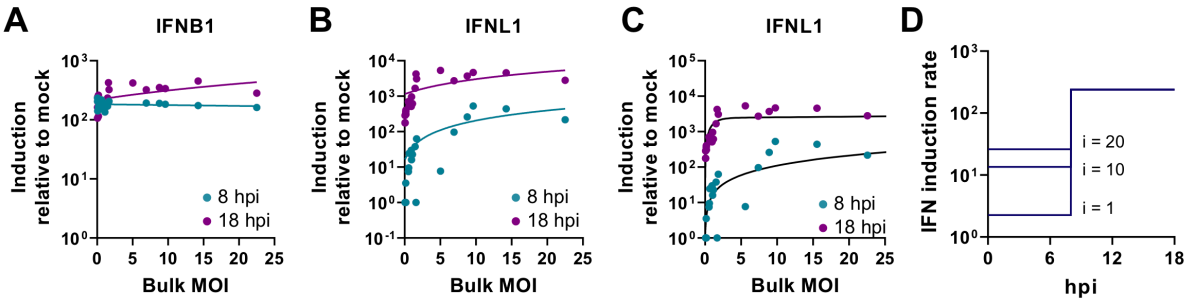

Fig. 4. Cellular co-infection enhances type III (but not type I) IFN induction. A549 cells were infected with PR8 under single cycle conditions at a range of bulk MOIs. Levels of cellular IFNB1 and IFNL1 transcript were measured by RT-qPCR at the indicated timepoints, compared to levels in mock cells, and plotted relative to actual MOI for each infection well. **(A)** IFNB1 induction at 8 hpi and 18 hpi. Based on log-log linear regression, significance of a non-zero slope for normalized IFNB1 level vs. actual MOI: 8 hpi, $p = 0.78$; 18 hpi, $p = 0.0002$. **(B)** IFNL1 induction at 8 hpi and 18 hpi, trend lines represent log-log linear regression with positive correlation between normalized IFNL1 induction and actual MOI at both timepoints ($p < 0.0001$). **(C)** Fit of the most preferred IFN induction model to 8 hpi and 18 hpi timepoint data(saturating input-dependent; solid line) that has the rate of IFNL1 induction scale linearly with viral input during the 0-8 hpi epoch and independent of viral input during the 8-18 hpi epoch. **(D)** Model predictions for the rate of IFNL1 induction over 0-8 hpi and 8-18 hpi epochs shown at different viral input levels (i = 1, 10, 20).

In contrast, we found a strong positive correlation between IFNL1 expression and bulk MOI at both 8 and 18 hpi ($p < 0.0001$ for both time points; **Fig. 4B**), although the effect was less pronounced at 18 hpi (slope = 0.58) compared with 8 hpi (slope = 1.28), suggesting that part of this effect could be due to input-dependent differences in activation kinetics. To determine whether the observed relationship between bulk MOI and IFNL1 induction could be explained simply as the result of increasing the number of infected cells, we statistically fit several mathematical models to these experimental data (Methods). Because only 8 hpi and 18 hpi data were available for model fitting, we considered different model combinations that pieced together a model governing the 0-8 hpi epoch with a model governing the 8-18 hpi epoch. During each epoch, we considered three different possible time-independent models: (1) an input-independent model (all infected cells had similar IFNL1 induction rates relative to mock cells), (2) an input-dependent model in which IFNL1 induction rates scaled linearly with virus input, and (3) an input-dependent model in which IFNL1 induction rates increased with virus input, with a saturating effect (**Table 3**). The statistical fits of these models jointly to the 8 hpi and 18 hpi IFNL1 induction data are shown in **Table 4**.

Table 3. Model descriptions of IFNL1 induction.

Model	IFN rate function	Parameter legend
(1) Input-independent	$\phi(t,i) = l$	l = IFNL1 induction rate (per hour), for all infected cells
(2) Linear input-dependent	$\phi(t,i) = r\,i$	r = slope of per virion induction rate (per hour)
(3) Saturating input-dependent	$\phi(t,i) = \frac{m\,i}{(K+i)}$	m = max induction rate (per hour) K = input at half max rate

Table 3. Model descriptions of IFNL1 induction. Rows show the three considered models. For each model, the table lists the functional form for the IFN induction rate ϕ (relative to mock-infected cells), with t representing time since infection (hpi) and i representing cellular input, and a description of the model parameters.

Table 4. IFNL1 induction models and their fit to data.

Model (0-8 hpi)	Parameter estimates	Model (8-18 hpi)	Parameter estimates	RSS	ΔAIC
1	$l = 3.394$	1	$l = 241.198$	110.7	20.8
1	$l = 3.431$	2	$r = 94.381$	128.1	26.8
1	$l = 3.394$	3	$m = 409.341$, $K = 1.269$	107.8	21.7
2	$r = 1.256$	1	$l = 238.626$	66.6	0
2	$r = 1.246$	2	$r = 95.481$	84.9	9.9
2	$r = 1.246$	3	$m = 396.116$, $K = 1.168$	64.2	0.5
3	$m = 1.256$, $K = 13.089$	1	$l = 238.626$	66.6	2.0
3	$m = 1.246$, $K = 11.425$	2	$r = 95.481$	84.9	11.9
3	$m = 1.246$, $K = 13.253$	3	$m = 228.669$, $K = 1.248$	64.1	2.4

Table 4. IFNL1 induction models and their fit to data. For each of the 9 possible model combinations (3 models for the 0-8hpi epoch x 3 models for the 8-18hpi epoch), the table shows the model parameter estimates, the residual sum of squares (RSS) of the parameterized model, and calculated ΔAIC values. For the calculations of ΔAIC, the number of data points is $n = 41$.

The most preferred combination, based on ΔAIC, is the linear input-dependence model during the 0-8 hpi epoch, coupled with the input-independent model during the 8-18 hpi epoch. As a close second lies the combination model with linear input-dependence during the 0-8 hpi epoch, coupled with the saturating input-dependent model during the 8-18 hpi epoch. However, the parameters of the 8-18 hpi saturating model are such that the input-dependence saturates at extremely low cellular MOI, effectively making this combination of models highly similar to the most preferred model. **Fig. 4C** shows the fit of the most preferred model combination to the IFNL1 8 hpi and 18 hpi data and **Fig. 4D** shows the IFNL1 induction rate (relative to mock) for this most preferred model. These statistical results indicate that, early on in infection, the rate (or probability) of IFNL1 induction depends on the extent of virus input, with cells with higher levels of virus input likely starting IFNL1 induction earlier than cells with lower levels of virus input. However, later in infection, the rate of IFNL1 induction appears to be insensitive to virus input.

Cellular co-infection decreases the potential for superinfection.

Finally, we wanted to understand what factors might regulate the potential for cellular co-infection. We previously showed that under low bulk MOI conditions, increasing the number of functional gene segments delivered to a given cell resulted in more potent superinfection exclusion (SIE), limiting the potential for cellular co-infection (20). We thus hypothesized that increases in cellular

MOI would shorten the time window during which superinfection is possible, thus limiting the total number of virions that can successfully infect a given cell.

To define how cellular MOI affects subsequent superinfection potential, we measured the extent of SIE across a range of bulk MOIs. We generated 2 antigenically distinct reassortant viruses (rH3N1 and rH1N2) that could be differentiated using specific monoclonal antibodies. We infected MDCK cells with rH3N1 at a range of intended MOIs resulting in groups with average bulk MOIs of 0.25, 1.13, 3.00, 15.43, and 53.72 TCID50/cell (based on subtracting post-adsorption inoculum GE titers from pre-adsorption inoculum titers as detailed above). At 6 hpi, we superinfected with a constant input MOI of rH1N2. To measure the baseline co-infection rates in the absence of SIE effects, we included co-infection controls for each input MOI where we simultaneously co-infected with rH3N1 and rH1N2 viruses. At 19 hpi, we examined the infection status of cells by flow cytometry, using N1 and H1 expression as markers of rH3N1 infection and rH1N2 infection, respectively.

As expected, during simultaneous co-infection (where no SIE occurs), we observed that the fraction of co-infected cells (H3+H1+) increased with the input MOI of rH3N1 virus and plateaued when almost all rH1N2-infected cells (H1+) were co-infected with rH3N1 (**Fig. 5A**). These simultaneous co-infection data allowed us to develop and parameterize an appropriate "null" model of co-infection in the absence of SIE. We first tested whether a simple model that assumed Poisson statistics could describe the data but found that it failed to reproduce key features of the co-infection data (Methods). Specifically, we found that the Poisson model predicted higher fractions of H3+ cells at high rH3N1 MOIs than what we observed (**Fig. S3**). We next considered a slightly more complicated model in which cells could differ in their susceptibility to viral infection. For simplicity's sake, we considered only two types of cells: ones with high susceptibility and ones with low susceptibility. Such variation in susceptibility could arise from a number of cell-intrinsic factors, including cell cycle stage. Once parameterized, this simple model was able to reproduce the experimental co-infection data extremely well (**Fig. 5A**).

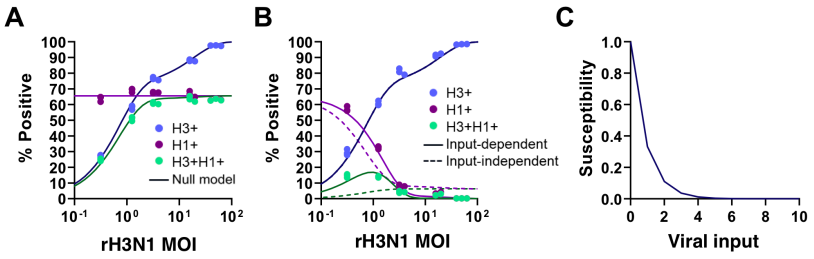

Fig. 5. Cellular co-infection decreases the potential for superinfection. (A) MDCK cells were simultaneously coinfected with rH1N2 (at a constant MOI) and rH3N1 (at varying input MOIs shown on the x-axis) under single cycle conditions; SIE would not be expected to occur during simultaneous coinfection. Plot shows the percentages of all cells infected with rH1N2 (H1+; includes co-infected cells), all cells infected with rH3N1 (H3+; includes co-infected cells), and cells coinfected with both (H3+H1+), as determined by flow cytometry at 19 hpi. Solid lines indicate the two-susceptibility state null model fit to these data. **(B)** MDCK cells were infected with rH3N1 at the varying input MOIs shown on the x-axis under single cycle conditions. 6 hours later, cells were superinfected with rH1N2 at a constant input MOI under single cycle conditions. Plot shows the percentages of all cells infected with rH1N2 (H1+; includes co-infected cells), all cells infected with rH3N1 (H3+; includes co-infected cells), and cells coinfected with both (H3+H1+), as determined by flow cytometry at 19 hpi. Statistical fits of the input-independent and input-dependent models are shown. **(C)** Model prediction of susceptibility to superinfection (with 1 being completely susceptible) as a function of viral input.

In contrast to what was observed under simultaneous co-infection conditions, under superinfection conditions we observed that the fractions of both double-infected (H3+H1+) cells and rH1N2-infected (H1+) cells decreased with increasing rH3N1 input MOI. To determine whether these patterns could simply be explained by higher numbers of cells being infected with rH3N1 at higher rH3N1 input MOIs, we assessed how well two different models of super-infection fit the experimental data (Methods). The first model assumed that all rH3N1-infected cells had the same reduced probability of becoming infected with rH1N2 (input-independent). The second model assumed that the probability of being infected with rH1N2 decreased with cellular rH3N1 MOI (input-dependent). We fit each of these two models to the SIE data (**Table 5**). The input-independent model systematically underestimated the extent of rH1N2 infection and of double (H3+H1+) infection at low rH3N1 input MOI, while systematically overestimating these measurements at high rH3N1 input MOI (**Fig. 5B**). In contrast, the input-dependent model was able to reproduce the measurements across all experimental MOIs without systematic over- or under-estimation (**Fig. 5B**). As anticipated from these patterns, we found that the input-dependent model was significantly better supported by the data than the input-independent model (ΔAIC = 62.7). **Fig. 5C** shows the relationship between cellular input and susceptibility to superinfection predicted by this input-dependent model, indicating a rapid decline in susceptibility to superinfection with rH1N2 at 6 hpi at increasing levels of rH3N1 virus input.

Table 5. Coinfection and superinfection exclusion models and their fit to data.

Model	Susceptibility of previously infected cells	Parameter estimates	RSS	ΔAIC	Parameter legend
Input-independent	$0 < s < 1$	$s = 0.043$	2096.1	62.7	s = susceptibility of previously infected cells (1 being fully susceptible)
Input-dependent	$0 < r^i < 1$, for $i = 1, 2, 3, \ldots$	$r = 0.332$	520.3	0	r = per virion susceptibility of previously infected cells

Table 5. Coinfection and superinfection exclusion models and their fit to data. Rows show the two considered models: an input-independent model and an input-dependent model. Each superinfection exclusion model estimated the value of only a single parameter (*s* or *r*), with three additional parameter values (rH1N2 input MOI, and fractions *x* and *y*) set based on the statistical fit of the simultaneous coinfection model to the coinfection data (**Fig. 5A**; Methods). For each SIE model, the table lists the functional form for cell susceptibility, with *i* representing cellular MOI. The table also lists model parameter estimates, the residual sum of squares (RSS) of the parameterized model, and calculated ΔAIC values. For the calculations of ΔAIC, the number of data points is n = 45.

These results are consistent with our previous finding that susceptibility to superinfection is inversely correlated with the cellular dosage of replication complexes delivered by incoming virions (20). Thus, the MOI-dependence of SIE may serve as a negative feedback loop that restricts the maximum number of virions that can successfully infect a given cell.

DISCUSSION

In this study we set out to define the functional consequences of cellular co-infection by quantifying the effects of cellular MOI on the phenotypes of infected cells. We combined precise, quantitative single-cycle *in vitro* infection experiments with statistical model fitting to demonstrate that at the cellular level, variation in viral input gives rise to substantial variation in infection outcomes. This includes variation in viral output dynamics as well as the host transcriptional

response to infection. Intriguingly, type I and type III IFN exhibited distinct responses to increases in MOI, suggesting that variation in cellular MOI could alter the balance of these two antiviral cytokines. Altogether, these results clearly establish the incidence of cellular co-infection as an important determinant of influenza virus infection outcome.

These results complicate the common understanding of viral genotype-phenotype relationships. Generally, we understand that the phenotype of a virus within a given host system is encoded by its genome sequence. Our data add another layer to this view: it is not simply the sequence(s) of a viral genome that influences its phenotype but also how those sequences are distributed across cells. Two viruses with identical genome sequences could exhibit significantly different replication dynamics if they differ in their cellular MOI distribution. These results suggest that we need to better understand the forces that govern the spatial distribution of virions and the extent of cellular co-infection during IAV infection.

Our findings also have implications for understanding reassortment potential. By definition, reassortant virus will be produced under conditions of cellular co-infection. If virus production by co-infected cells is faster and more efficient than that of singly infected cells, reassortant progeny would have a numeric advantage over parental genotype viruses independent of any inherent fitness differences, purely based on the conditions under which they are produced. This effect could contribute to the high frequency reassortment that has been observed in multiple experimental settings (21,22).

The IFN system represents one of the earliest and most potent lines of defense against IAV within the respiratory tract (23–25). Similar to previous reports, we observed that IAV infection resulted in a more dramatic induction of type III IFN (26), compared with type I IFN. We were surprised to find that type I and type III IFN induction responded differently to increases in input MOI, as the induction pathways that lead to initiation of IFNB1 and IFNL1 are thought to largely overlap (27). Our data suggest that the induction or regulatory circuitry for these two pathways are differentially affected by the amount of viral input. Even more surprising was our finding that type I IFN induction was largely insensitive to input MOI over two orders of magnitude. In our hands, not only was IFNB1 induction MOI-independent at the cellular level, it was also largely unaffected by the total number of infected cells, which ranged from ~3% to ~63% across the samples tested. Induction of IFNB1 expression by IAV is known to be highly stochastic at the single cell level and many infected cells do not upregulate IFN expression (14,28,29); however, it is still counterintuitive that increasing the total number of infected cells would not increase the overall number of cell producing IFNB1 (and thus the bulk expression level). More work is clearly needed to understand the factors that govern IFN expression at the single cell level.

The implications of these results for understanding what happens during natural infection remain unclear, but at a minimum suggest that frequent occurrence of cellular co-infection is likely to boost the magnitude of the type III, but not the type I IFN response. This dynamic could lead to MOI-dependent changes in the relative balance of type I versus type III IFN induction which could be consequential given that these cytokine families can trigger non-redundant effector responses during IAV infection (30–33). One important caveat here is that we are only examining IFN induction within a single cycle of replication and a single cell type and patterns of type I and type III IFN induction over the course of infection are sure to be much more complicated.

It is also important to point out that the experimental data described here were all collected from aggregate populations of cells and that our models ignore single cell heterogeneity between cells

with the same cellular MOI. It is clear that there is substantial heterogeneity in viral gene expression and progeny production between individual cells infected under similar conditions (29,34,35). Time-course experiments from single poliovirus-infected cells have demonstrated that bulk measurements like those used here can obscure more complex, heterogeneous dynamics that occur at the single cell level (36). A more complete understanding of the functional consequences of cellular co-infection will likely depend upon future studies that quantify single cell variability.

Given that cellular MOI and co-infection have clear functional consequences during IAV infection, it is critical to quantify the actual occurrence of cellular co-infection during *in vivo* infection and to identify host and viral determinants of cellular co-infection frequency. Natural infections are likely typically initiated under low MOI conditions due to the relatively small size of transmitted founder populations (though even small numbers of transmitted virions could achieve high cellular MOI if they are physically aggregated) (37,38). Even if infection is initiated at low cellular MOI, high cellular MOI conditions could be very rapidly established if viral spread is locally restricted, as appears to be the case (7). This idea is supported by a recent study that demonstrated that a virus that is entirely dependent upon cellular co-infection to replicate can successfully replicate in guinea pigs (39). Though very few studies have attempted to actually quantify the MOI distribution *in vivo* because of the inherent technical challenges, our work suggests that this feature could be an important, underappreciated determinant of infection outcome.

Our finding that cellular co-infection can enhance replication efficiency and speed suggests that, under some circumstances, increasing the frequency of co-infection could be adaptive. For example, by accelerating virus production, co-infection could help the virus outrun the host innate immune response. Such a dynamic would mirror the findings of a recent study of vesicular stomatitis virus that demonstrated that virion aggregation could enhance viral fitness by increasing co-infection rates (40). Notably, the authors observed that the fitness advantages conferred by aggregation were significantly more pronounced in cell lines with more intact antiviral defenses, suggesting a central role for immune evasion in this effect.

This study also highlights the power of interfacing carefully quantified experimental data with dynamic statistical modeling approaches. By fitting models to our experimental data, we were able to rigorously test our hypotheses concerning the phenotypic effects of cellular MOI to an extent that would not be possible based on standard data analysis. This was essential for confidently distinguishing between the different functional forms that could potentially describe the phenotypic consequences of different levels of virus input. Hopefully, the data generated here will help inform future mathematical modeling efforts focused on understanding IAV within-host infection dynamics. Our results to date certainly suggest that future model structures may better capture the underlying biology of IAV infection if they account for the phenotypic consequences of cellular co-infection (41,42).

Altogether, our results clearly demonstrate that cellular MOI can have concrete effects on infection outcome, highlighting the functional importance of collective interactions during IAV infection (43). At a minimum, our data establish that the distribution of viral genomes across cells and the patterns of cellular co-infection that result can significantly alter emergent viral infection phenotypes. This suggests that future efforts to understand influenza virus infection dynamics and outcomes should consider patterns of virus input and cellular co-infection.

MATERIALS AND METHODS

430 **Cells**
431 HEK293T (human embryonic kidney) cells were used for rescue of PR8 by plasmid transfection.
432 MDCK (Madin-Darby canine kidney) cells were used for virus propagation, $TCID_{50}$, and infection
433 experiments. 293T and MDCK were maintained in MEM (Thermo Fisher Scientific; Waltham, MA,
434 USA) supplemented with 8.3% fetal bovine serum (FBS). A549 (human lung carcinoma) cells
435 were used for infection experiments and were maintained in Ham's F12 nutrient mixture (Thermo
436 Fisher Scientific; Waltham, MA, USA) with 8.3% FBS.
437
438 **Virus rescue and propagation**
439 Eight plasmids encoding the A/Puerto Rico/8/1934 (H1N1; PR8) segments PB2, PB1, PA, HA,
440 NP, NA, MA, and NS in the dual promoter pDZ vector were used to generate recombinant virus
441 stocks through standard IAV reverse genetics. The recombinant PR8 virus (rPR8) differs from the
442 published sequence (GenBank accession nos. AF389115–AF389122) at two positions: PB1
443 A549C (K175N) and HA A651C (I207L) (numbering from initiating Met). rH3N1 and rH1N2 viruses
444 used in superinfection studies were similarly generated through reverse genetics, using the HA
445 and NA segments from A/Udorn/307/72 (H3N2) respectively and the remaining segments from
446 PR8.
447
448 For virus rescue, 500 ng of each plasmid were mixed with 200 μL jetPRIME buffer (Polyplus-
449 transfection; Illkirch, France) and 8 μL jetPrime reagent and incubated at room temperature for
450 10 minutes. The transfection mixture was added dropwise to 293T cells at 60% confluency in 6-
451 well cell culture plates and incubated at 37ºC, 5% CO2. Media was changed 18-24 hours post-
452 transfection, with 2 mL of virus growth media (MEM, 1 mM HEPES, 1 μg/mL TPCK trypsin
453 (Worthington Biochemical Corporation; Lakewood, NJ, USA), 50 μg/mL gentamicin) containing
454 2×10^5 MDCK cells. Rescue supernatant was harvested and used in plaque assay. Briefly, 300 μl
455 10-fold serially diluted transfection supernatant in 1X DPBS (+Ca/+Mg), 0.1% BSA, pH 7.1, was
456 added per 100% confluent MDCK well in 6-well cell culture plate, in duplicate. After 1 hour of
457 incubation, 3 mL agarose overlay (0.9% agarose, 1X EMEM, 1 μg/mL TPCK trypsin, 0.2% BSA,
458 1X glutamax, 1 mM HEPES, 50 μg/mL gentamicin) was added to each well and incubated for 48-
459 72 hours at 37ºC.
460
461 To generate seed virus stocks, three isolated plaques were picked and resuspended in 200μL 1X
462 DPBS (+Ca/+Mg), 0.1% BSA; 100 μL was added to one well of 6-well cell culture plate with 80%
463 confluent MDCK cells with 2 mL of virus growth media and incubated at 37ºC, 5% CO2 for 48-72
464 hours. To generate working stock virus, confluent MDCK cells were infected with seed virus stock
465 at an MOI of 0.001 TCID50. One-hour post infection, inoculum was discarded and replaced with
466 virus growth media and incubated at 37ºC, 5% CO2 for 48-72 hours. Supernatant was clarified at
467 3000 RPM for 10 minutes and 500 μL aliquots were stored at -70ºC.
468
469 50% tissue culture infective dose ($TCID_{50}$) for PR8 viral supernatant was titrated in 96-well cell
470 culture plates with 100% confluent MDCK cells by 1:10 serial dilution in virus growth media.
471 Cytopathic effect was visualized 3-5 days post infection. $TCID_{50}$ values were calculated based on
472 Reed and Munch calculation(44).
473
474 **Viral output assay**
475 To precisely quantify the effects of viral input on viral output and cell death rates, PR8 was diluted
476 in 1X PBS +/+ pH 7.3 in 200 μL triplicates to yield intended MOIs of 0.25, 1, 2.5, 5, and 25 and
477 used to inoculate MDCK or A549 cells in 24-well plates. Infections were synchronized by carrying
478 out adsorption at 4ºC for 1 hour. The supernatant was collected at 1 hpi, the cell monolayers were

479 washed three times with 1X PBS, media was replaced with 500 μL MEM or F12, for MDCK and
480 A549 respectively, with 8.3% FBS and cells were shifted to 37ºC. At 2 hpi, media was
481 supplemented with 20 mM NH_4Cl to block secondary spread of the virus (45). Total viral
482 supernatant was collected at 3, 6, 12, and 18 hpi and stored for at -70ºC for later use. Cell
483 monolayers were then trypsinized and either stained with trypan blue and manually counted with
484 a bright-line hemocytometer (to quantify remaining live cells) or prepared directly for flow
485 cytometry.
486
487 **Measurement of viral genome equivalents by RT-qPCR**
488 Viral RNA was isolated from viral supernatant with Zymo vRNA 96-well extraction kit (Zymo
489 Research; Irvine, CA, USA) according to manufacturer's instructions, eluted with 30 μL RNase
490 free water, and stored at -70ºC. For cDNA synthesis, 5 μL vRNA, 0.5 μL 10 mM dNTP mix (Sigma-
491 Aldrich), and 1.0 μL Uni12(46) (AGCAAAAGCAGG) were incubated at 65ºC for 5 minutes then
492 transferred to ice for 2 minutes. 1 μL SUPERase In RNase inhibitor (20 U/μL; Thermo Fisher
493 Scientific; Waltham, MA, USA) was added to each mixture and incubated on ice again for 2
494 minutes. 6.5 μL dH_2O, 4 μL 5X First-Strand Buffer, 1 μL 100 mM DTT, and 1 μL SuperScript III
495 RT (200 U/μL; Thermo Fisher Scientific; Waltham, MA, USA) were added to each reaction and
496 incubated at 55ºC for 60 minutes and heat inactivated at 70ºC for 15 minutes.
497
498 Genome equivalents (GE) were estimated by RT-qPCR of MA gene segment. In duplicate for
499 each sample, 10 μL Power SYBR Green PCR master mix (Thermo Fisher Scientific; Waltham,
500 MA, USA), 0.5 μL 10 μM forward and reverse primers (MA-Forward:
501 ACAGAGACTTGAAGATGTC and MA-Reverse: TCTTTAGCCATTCCATGAG), 8 μL dH_2O, and
502 1 μL cDNA were added to 0.2 mL MicroAmp Optical 96-well reaction plate (Thermo Fisher
503 Scientific; Waltham, MA, USA). RT-qPCR was performed on the QuantStudio 3 (Thermo Fisher
504 Scientific; Waltham, MA, USA) platform and the cycling conditions were as follows: 95ºC for 10
505 minutes, 40 cycles of 95ºC for 15 seconds and 60ºC for 60 seconds. The standard curve
506 established with pDZ-PR8 MA plasmid (R^2 of 0.9992) was used to estimate GE/μL and then each
507 sample was corrected for dilution factor to give a final GE/mL.
508
509 **Superinfection assay**
510 For the 6hr superinfection group, confluent MDCK cells in six-well plates were infected with rH3N1
511 virus at intended MOIs of 0.05, 0.25, 1, 2.5, and 10 TCID50/cell respectively at 4°C. 1 hour post-
512 adsorption, remaining inoculum was collected, monolayers were washed with PBS and incubated
513 in MEM + 8.3% FBS. At 6 hpi, monolayers were superinfected with rH1N2 at MOI=0.5 TCID50/cell
514 at 4°C. 1 hour post-adsorption, monolayers were washed with PBS and incubated in MEM + 8.3%
515 FBS. At 9 hpi of rH3N1 (3 hpi of rH1N2), the media was changed to MEM with 50 mM HEPES
516 and 20 mM NH4Cl to block spread of both viruses. For the 0hr co-infection group, cells were
517 infected with a mixture of rH3N1 and rH1N2 at the same MOIs as in 6hr superinfection group. At
518 3 hpi, 20 mM NH4Cl was added to block viral spread. For both 0hr and 6hr groups, at 19 hpi of
519 rH3N1 (13 hpi of rH1N2), cell monolayers were trypsinized into single-cell suspensions and
520 stained with Alexa Fluor 647-conjugated mouse anti-N1 mAb NA2-1C1 and Alexa Fluor 488-
521 conjugated mouse anti-H1 mAb H28-E23 (gifts of Dr. Jon Yewdell). After staining, cells were
522 washed with PBS, run on a BD LSR II, and analyzed using FlowJo version 10.1 (Tree Star, Inc.).
523 To quantify actual MOIs, virus present in both pre- and post-adsorption inoculum was quantified
524 by RT-qPCR as above using the following primers specific for the N1 segment:
525 AAATCAGAAAATAACAACCATTGGA, ATTCCCTATTTGCAATATTAGGCT.
526
527 **Interferon quantification**

528 The quantification of interferon ß1 (IFNB1) and interferon λ1 (IFNL1) induction was quantified
529 during infection of A549 cells with PR8 at intended MOIs of 0.1-100. In brief, A549 cells in 24-well
530 plate were inoculated for one-round of replication, as described previously. At 8 or 18 hpi,
531 supernatant was removed, cells were washed thoroughly, dissociated from the plate, and cellular
532 mRNA was extracted with RNeasy Mini kit (QIAGEN Hilden, Germany), according to
533 manufacturer's instructions. Reverse transcription was completed with SuperScript III first-strand
534 synthesis system for RTq-PCR (Thermo Fisher Scientific; Waltham, MA, USA). Briefly, 8 μL
535 cellular mRNA was incubated with 2.5 ng/μL random hexamers, and 0.5 nM dNTP mix at 65ºC
536 for 5 minutes then placed on ice for 1 minute. Then 1X RT buffer, 5 mM $MgCl_2$, 0.01 M DTT, 2
537 U/μL RNaseOUT, and 10 U/μL SuperScript III RT were added to each sample and incubated at
538 25ºC for 10 minutes, 50ºC for 50 minutes, and 85ºC for 5 minutes; finally 1 μL RNase H was
539 added and incubated at 37ºC for 20 minutes. With cellular cDNA, TaqMan gene expression
540 assays (FAM-MGB; Thermo Fisher Scientific; Waltham, MA, USA) specific for IFNB1 and IFNL1
541 were used in multiplex with TaqMan GAPDH control reagents kit (JOE-TAMRA; Thermo Fisher
542 Scientific; Waltham, MA, USA). Briefly, in duplicate 2μL cellular cDNA was added to 2 μL TaqMan
543 Fast Advanced Master Mix, 1 μL either IFNB1 or IFNL1 TaqMan Gene expression assay, 100 nM
544 GAPDH forward and reverse primers, 200 nM GAPDH TaqMan probe, and dH_2O in 20 μL. RTq-
545 PCR was performed on the QuantStudio 3 platform and the cycling conditions were as follows:
546 95ºC for 20 seconds, 40 cycles of 95ºC for 1 second and 60ºC for 20 seconds. Induction of IFN
547 was quantified by the fold change of IFN in infected cells from mock infected cells.
548
549 **Statistical modeling of cell death**
550 For the statistical modeling of cell death, we asked whether death rates of infected cells depended
551 upon virus input. We also used the time course data to assess whether there was time-
552 dependency in the cell death rate. We used a residual sum of squares (RSS) approach to fit all
553 cell death models considered and relied on the Akaike Information Criterion (AIC) for selecting
554 between alternative models. Table 1 shows all considered cell death model fits. All cell death
555 models considered assumed that virus input was distributed across cells according to a Poisson
556 distribution, with the mean given by the precisely quantified actual input MOI. We first considered
557 the simplest possible model: a model that assumed that cell death rates were the same across
558 all infected cells and that cell death rates did not change over the course of a cell's infection.
559 Across bulk MOIs, this model overestimated the fraction of surviving cells early in infection and
560 underestimated this fraction late in infection. Due to these systematic biases, we next considered
561 a cell death model that was time-dependent, but independent of virus input. Specifically, we let
562 the cell death rate be given by a Weibull hazard function, a common approach for integrating time-
563 dependency into death rate estimation. The Weibull hazard function is a two-parameter model (b,
564 k), with direct interpretation possible from the estimated shape parameter k. The estimate of $k <$
565 1 (Table 1) indicates that the "failure rate" is decreasing over time, with cell death rates being high
566 initially and decreasing over the course of infection. This model was able to reproduce the patterns
567 in the experimental data without any systematic over- or underestimation of data points either
568 across bulk MOIs or over time. Finally, we fit a model that allowed infected cells to have different
569 cell death rates, depending on their virus input. All cells infected with a certain number of particles
570 were assumed to have a death rate that did not change over the course of infection. For this
571 model, we specifically assumed that cell death rates increased linearly with cellular MOI. This
572 model overestimated the fraction of surviving cells at low input MOI conditions and
573 underestimated this fraction at high input MOI. Based on AIC, the time-dependent (Weibull hazard
574 function), input-independent model was stronger preferred over the two other models considered
575 (**Table 1**).
576

577 **Statistical modeling of virus production**
578 For the statistical modeling of virus production, we asked whether rates of virus production from
579 a cell were dependent on its cellular MOI. Because we had experimental data from various points
580 in time (6, 12, and 18 hpi), we could further ask whether virus production rates have a time-
581 dependent component. All virus production models considered assumed that virus input was
582 distributed across cells according to a Poisson distribution, with the mean given by the precisely
583 quantified input MOI. We first fit the simplest possible model: a model that assumed a single
584 constant rate of virus production from all infected cells (**Table 2**). In fitting this model, we
585 incorporated the effect of cell death, since the number of infected cells remaining decreased over
586 time due to infected cell death. Specifically, we assumed a Weibull hazard function for the cell
587 death rate, parameterized with values shown in Table 1. The second (time-independent) model
588 we fit assumed that virus production rates scaled linearly with cellular MOI but did not change
589 over the course of a cell's infection. The third model we fit assumed that virus production rates
590 increased with cellular MOI, ultimately saturating at high virus input. Specifically, we used a
591 Michaelis-Menten functional form to accommodate this saturation effect. Again, for this model, we
592 assumed that virus production rates did not change over the course of infection. Parameter
593 estimates for each of these three time-independent models are shown in Table 2. Fig S2 shows
594 that all three of these models overestimated virus output early on in infection (6 hpi) and
595 underestimated virus output late in infection (18 hpi).
596
597 Due to these time-dependent model biases, we moved to considering time-dependent models
598 (**Table 2**). We assumed in these models that virus production rates increase linearly with time,
599 starting at a set time point. The first time-dependent model we fit further assumed that all infected
600 cells had similar virus production rates. This model overestimated virus output at low input MOI
601 and underestimated virus output at high input MOI. The next time-dependent model we
602 considered was a model in which virus production rates further scaled linearly with virus input.
603 Finally, we considered a time-dependent model in which virus production rates were governed by
604 a Michaelis-Menten saturating form that depended on cellular MOI. Both of these latter two time-
605 dependent models appeared to perform well, with predictions that did not exhibit systematic
606 biases across time points or experimental MOI conditions. Based on AIC (**Table 2**), the time-
607 dependent, input-dependent Michaelis-Menten model outperformed the other 5 models.
608
609 **Statistical modeling of the interferon response**
610 For the statistical modeling of IFN induction, we asked whether the rate of IFN induction from a
611 cell was dependent on cellular MOI. We only fit models to the IFNL1 data because a strong
612 positive relationship between the fraction of infected cells and IFNB1 induction levels was not
613 apparent in the IFNB1 data. IFN induction levels (relative to mock-infected cells) were quantified
614 across experimental MOIs at 8 hpi and 18 hpi. Because only two time point measurements were
615 available and because there was considerable noise apparent in the 8 hpi measurements, we fit
616 the available data using a piecewise approach (instead of considering both time-independent and
617 time-dependent models). We again assumed that virus input was distributed across cells
618 according to a Poisson distribution, with the mean given by the precisely quantified input MOI.
619 Any IFNL1 induction measurements that fell below the mock-infected IFNL1 level we set to 1
620 (same as mock-infected) as these are likely due to experimental noise given the low baseline
621 expression of IFNL1 in mock cells. Infected cells were assumed to die at a rate given by the
622 parameterized Weibull hazard function (**Table 1**). The piecewise approach to fitting the data
623 assumed that between 0 and 8 hpi, IFN induction occurred at a rate that was constant in time but
624 could depend on cellular MOI. Similar to the virus output model, we considered three possible
625 virus input dependencies (all relative to mock-infected cells): (1) IFN induction was the same

626 across all infected cells; (2) IFN induction scaled linearly with cellular MOI; and (3) the level of
627 IFN induction was governed by a saturating Michaelis-Menten function that depended on cellular
628 MOI (**Table 3**). Similarly, we assumed that IFN induction occurred at a constant rate between 8
629 and 18 hpi, with these three possible virus input dependencies. The IFN induction rate between
630 0-8 hpi could differ from the one between 8-18 hpi. **Table 4** shows the fits of the 9 distinct models
631 that are possible (3 models during the 0-8 hpi epoch x 3 models during the 8-18 hpi epoch). Based
632 on AIC, the most preferred model was the combination of models that had linear input-
633 dependence in the 0-8 hpi epoch and constant input-dependence in the 8-18 hpi epoch.
634
635 **Statistical modeling of superinfection exclusion**
636 We first developed and parameterized an appropriate 'null' model, where both viruses are
637 introduced simultaneously and superinfection exclusion would not be anticipated. We first
638 considered whether a simple model assuming Poisson statistics would be consistent with the
639 observed data. Under this model, we estimated only the input MOI of rH1N2. This model could
640 not reproduce key features in the observed coinfection data (**Fig. S3**): at the precisely measured
641 input rH3N1 MOIs, the Poisson model yielded expectations of higher percentages of H3
642 expressing cells than those observed, particularly at high rH3N1 input MOIs.
643
644 We thus assumed that cells differed in their susceptibility to viral infection. As the simplest starting
645 model, we considered only two types of cells: ones that had high susceptibility to infection and
646 ones that had low susceptibility to infection. We defined fraction y of the cell population to be in
647 low susceptibility state; the remaining fraction $(1-y)$ we assumed was in a high susceptibility state.
648 We let a fraction x of the viral population enter the low susceptibility state cells; the remaining
649 fraction of the viral population $(1-x)$ we assumed entered the high susceptibility state cells. Under
650 this model, the MOI of specifically the low susceptibility class of cells is given by (input MOI)*(x/y),
651 and the MOI of specifically the high susceptibility class of cells is given by (input MOI)*$(1-x)/(1-y)$.
652 When $x = y$, the Poisson distribution assumption is recovered, and both classes of cells have the
653 same input MOI. We fit this simple model to the coinfection data, estimating three parameters:
654 the actual rH1N2 MOI, and the fractions x and y. The parameter values, estimated using an RSS
655 approach, are actual rH1N2 MOI = 1.53, $x = 0.0147$, and $y = 0.2760$). This parameterized model
656 was able to reproduce the experimental data extremely well, without any apparent systematic
657 biases (**Fig. 5A**).
658
659 To analyze the data from the superinfection experiment, we set as given the three parameter
660 values and simple two-state susceptibility model structure derived from the fitting of the data from
661 the simultaneous coinfection experiment described above. We then considered two distinct
662 models to determine how cellular MOI may impact the rate of superinfection exclusion: an input-
663 independent model and an input-dependent model. The input-independent model assumed that
664 all infected cells had the same lower chance of being superinfected than previously uninfected
665 cells. The parameter s quantified the extent of susceptibility of the previously infected cells (1
666 being full susceptibility). The input-dependent model instead assumed that cells that were infected
667 with rH3N1 could experience different probabilities of superinfection exclusion. These different
668 probabilities depended on a rH3N1 virus input, with, presumably, higher levels of rH3N1 virus
669 input corresponding to higher probabilities of superinfection exclusion. For the input-dependent
670 model, we specifically assumed a functional form given by r^i , where i denotes rH3N1 virus input
671 and $0 \leq r \leq 1$. Estimated parameter values for s and r are shown in **Table 4**. The input-
672 independent model underestimates the fraction of cells that are double (H3+H1+) infected at low
673 input MOI and overestimates this fraction at high input MOI. In contrast, the input-dependent
674 model reproduces the experimental data across all experimental rH3N1 input MOIs (**Fig. 5B**).

Based on AIC, the input-dependent model is strongly preferred over the input-independent model (**Table 4**).

All statistical modeling code will be made available on GitHub following publication.

ACKNOWLEDGMENTS

Work in the Brooke and Koelle labs on this study was generously supported by DARPA-16-35-INTERCEPT-FP-018. The Brooke lab was further supported by 1R01AI139246-01A1 on this study.

REFERENCES

1. Lowen AC. Constraints, Drivers, and Implications of Influenza A Virus Reassortment. Annu Rev Virol. 2017 Sep 29;4(1):105–21.

2. Brooke CB, Ince WL, Wrammert J, Ahmed R, Wilson PC, Bennink JR, et al. Most influenza a virions fail to express at least one essential viral protein. J Virol. 2013 Mar;87(6):3155–62.

3. Diefenbacher M, Sun J, Brooke CB. The parts are greater than the whole: the role of semi-infectious particles in influenza A virus biology. Curr Opin Virol. 2018 Jul 24;33:42–6.

4. Brooke CB. Population Diversity and Collective Interactions during Influenza Virus Infection. J Virol. 2017 Nov 15;91(22).

5. Brooke CB, Ince WL, Wei J, Bennink JR, Yewdell JW. Influenza A virus nucleoprotein selectively decreases neuraminidase gene-segment packaging while enhancing viral fitness and transmissibility. Proc Natl Acad Sci U S A. 2014 Nov 25;111(47):16854–9.

6. Fukuyama S, Katsura H, Zhao D, Ozawa M, Ando T, Shoemaker JE, et al. Multi-spectral fluorescent reporter influenza viruses (Color-flu) as powerful tools for *in vivo* studies. Nat Commun. 2015 Mar 25;6:6600.

7. Gallagher ME, Brooke CB, Ke R, Koelle K. Causes and Consequences of Spatial Within-Host Viral Spread. Viruses. 2018 13;10(11).

8. Walsh JJ, Dietlein LF, Low FN, Burch GE, Mogabgab WJ. Bronchotracheal response in human influenza. Type A, Asian strain, as studied by light and electron microscopic examination of bronchoscopic biopsies. Arch Intern Med. 1961 Sep;108:376–88.

9. Guarner J, Shieh WJ, Dawson J, Subbarao K, Shaw M, Ferebee T, et al. Immunohistochemical and in situ hybridization studies of influenza A virus infection in human lungs. Am J Clin Pathol. 2000 Aug;114(2):227–33.

10. van den Brand JMA, Stittelaar KJ, van Amerongen G, Reperant L, de Waal L, Osterhaus ADME, et al. Comparison of temporal and spatial dynamics of seasonal H3N2, pandemic H1N1 and highly pathogenic avian influenza H5N1 virus infections in ferrets. PloS One. 2012;7(8):e42343.

713 11. Osterlund P, Strengell M, Sarin LP, Poranen MM, Fagerlund R, Melen K, et al. Incoming
714 Influenza A Virus Evades Early Host Recognition, while Influenza B Virus Induces
715 Interferon Expression Directly upon Entry. J Virol. 2012 Oct 15;86(20):11183–93.

716 12. White DO, Cheyne IM. Early events in the eclipse phase of influenza and parainfluenza
717 virus infection. Virology. 1966 May;29(1):49–59.

718 13. White DO, Day HM, Batchelder EJ, Cheyne IM, Wansbrough AJ. DELAY IN THE
719 MULTIPLICATION OF INFLUENZA VIRUS. Virology. 1965 Feb;25:289–302.

720 14. Ramos I, Smith G, Ruf-Zamojski F, Martinez-Romero C, Fribourg M, Carbajal EA, et al.
721 Innate immune response to influenza virus at single-cell resolution in human epithelial cells
722 revealed paracrine induction of interferon lambda 1. J Virol. 2019 Aug 2;

723 15. Martin K, Helenius A. Nuclear transport of influenza virus ribonucleoproteins: the viral
724 matrix protein (M1) promotes export and inhibits import. Cell. 1991 Oct 4;67(1):117–30.

725 16. Furuta Y, Takahashi K, Kuno-Maekawa M, Sangawa H, Uehara S, Kozaki K, et al.
726 Mechanism of action of T-705 against influenza virus. Antimicrob Agents Chemother. 2005
727 Mar;49(3):981–6.

728 17. Dou D, Hernández-Neuta I, Wang H, Östbye H, Qian X, Thiele S, et al. Analysis of IAV
729 Replication and Co-infection Dynamics by a Versatile RNA Viral Genome Labeling Method.
730 Cell Rep. 2017 Jul;20(1):251–63.

731 18. Phipps KL, Ganti K, Carnaccini S, Manandhar M, Jacobs NT, Pickett BE, et al. Collective
732 interactions augment influenza A virus replication in a host-dependent manner. bioRxiv
733 [Internet]. 2019 Aug 15 [cited 2019 Aug 21]; Available from:
734 http://biorxiv.org/lookup/doi/10.1101/736108

735 19. Jacobs NT, Onuoha NO, Antia A, Steel J, Antia R, Lowen AC. Incomplete influenza A virus
736 genomes occur frequently but are readily complemented during localized viral spread. Nat
737 Commun. 2019 Aug 6;10(1):3526.

738 20. Sun J, Brooke CB. Influenza A Virus Superinfection Potential Is Regulated by Viral
739 Genomic Heterogeneity. Denison MR, editor. mBio [Internet]. 2018 Oct 30 [cited 2019 May
740 2];9(5). Available from: http://mbio.asm.org/lookup/doi/10.1128/mBio.01761-18

741 21. Marshall N, Priyamvada L, Ende Z, Steel J, Lowen AC. Influenza Virus Reassortment
742 Occurs with High Frequency in the Absence of Segment Mismatch. Basler CF, editor.
743 PLoS Pathog. 2013 Jun 13;9(6):e1003421.

744 22. Tao H, Li L, White MC, Steel J, Lowen AC. Influenza A Virus Coinfection through
745 Transmission Can Support High Levels of Reassortment. J Virol. 2015 Aug;89(16):8453–
746 61.

747 23. Iwasaki A, Pillai PS. Innate immunity to influenza virus infection. Nat Rev Immunol. 2014
748 May;14(5):315–28.

749 24. Everitt AR, Clare S, Pertel T, John SP, Wash RS, Smith SE, et al. IFITM3 restricts the
750 morbidity and mortality associated with influenza. Nature. 2012 Mar 25;484(7395):519–23.

751 25. Killip MJ, Fodor E, Randall RE. Influenza virus activation of the interferon system. Virus
752 Res. 2015 Nov 2;209:11–22.

753 26. Österlund P, Strengell M, Sarin LP, Poranen MM, Fagerlund R, Melén K, et al. Incoming
754 Influenza A Virus Evades Early Host Recognition, while Influenza B Virus Induces
755 Interferon Expression Directly upon Entry. J Virol. 2012 Oct 15;86(20):11183–93.

756 27. Lazear HM, Schoggins JW, Diamond MS. Shared and Distinct Functions of Type I and
757 Type III Interferons. Immunity. 2019 Apr 16;50(4):907–23.

758 28. Killip MJ, Jackson D, Pérez-Cidoncha M, Fodor E, Randall RE. Single-cell studies of IFN-β
759 promoter activation by wild-type and NS1-defective influenza A viruses. J Gen Virol. 2017
760 Mar;98(3):357–63.

761 29. Russell AB, Elshina E, Kowalsky JR, Te Velthuis AJW, Bloom JD. Single-cell virus
762 sequencing of influenza infections that trigger innate immunity. J Virol. 2019 May 8;

763 30. Galani IE, Triantafyllia V, Eleminiadou E-E, Koltsida O, Stavropoulos A, Manioudaki M, et
764 al. Interferon-λ Mediates Non-redundant Front-Line Antiviral Protection against Influenza
765 Virus Infection without Compromising Host Fitness. Immunity. 2017 16;46(5):875-890.e6.

766 31. Klinkhammer J, Schnepf D, Ye L, Schwaderlapp M, Gad HH, Hartmann R, et al. IFN-λ
767 prevents influenza virus spread from the upper airways to the lungs and limits virus
768 transmission. eLife [Internet]. 2018 Apr 13 [cited 2019 Jun 25];7. Available from:
769 https://elifesciences.org/articles/33354

770 32. Hemann EA, Green R, Turnbull JB, Langlois RA, Savan R, Gale M. Interferon-λ modulates
771 dendritic cells to facilitate T cell immunity during infection with influenza A virus. Nat
772 Immunol [Internet]. 2019 Jun 24 [cited 2019 Jun 26]; Available from:
773 http://www.nature.com/articles/s41590-019-0408-z

774 33. Forero A, Ozarkar S, Li H, Lee CH, Hemann EA, Nadjsombati MS, et al. Differential
775 Activation of the Transcription Factor IRF1 Underlies the Distinct Immune Responses
776 Elicited by Type I and III Interferons. Immunity [Internet]. 2019 Aug [cited 2019 Aug 27];
777 Available from: https://linkinghub.elsevier.com/retrieve/pii/S1074761319303231

778 34. Russell AB, Trapnell C, Bloom JD. Extreme heterogeneity of influenza virus infection in
779 single cells. eLife [Internet]. 2018 Feb 16 [cited 2018 Mar 15];7. Available from:
780 https://elifesciences.org/articles/32303

781 35. Heldt FS, Kupke SY, Dorl S, Reichl U, Frensing T. Single-cell analysis and stochastic
782 modelling unveil large cell-to-cell variability in influenza A virus infection. Nat Commun.
783 2015 Nov 20;6:8938.

784 36. Guo F, Li S, Caglar MU, Mao Z, Liu W, Woodman A, et al. Single-Cell Virology: On-Chip
785 Investigation of Viral Infection Dynamics. Cell Rep. 2017 Nov;21(6):1692–704.

786 37. Varble A, Albrecht RA, Backes S, Crumiller M, Bouvier NM, Sachs D, et al. Influenza A
787 virus transmission bottlenecks are defined by infection route and recipient host. Cell Host
788 Microbe. 2014 Nov 12;16(5):691–700.

789 38. McCrone JT, Woods RJ, Martin ET, Malosh RE, Monto AS, Lauring AS. Stochastic
790 processes constrain the within and between host evolution of influenza virus. eLife
791 [Internet]. 2018 May 3 [cited 2019 Jan 7];7. Available from:
792 https://elifesciences.org/articles/35962

793 39. Jacobs NT, Onuoha NO, Antia A, Antia R, Steel J, Lowen AC. Incomplete influenza A virus
794 genomes are abundant but readily complemented during spatially structured viral spread.
795 bioRxiv [Internet]. 2019 Jan 23 [cited 2019 May 6]; Available from:
796 http://biorxiv.org/lookup/doi/10.1101/529065

797 40. Andreu-Moreno I, Sanjuán R. Collective Infection of Cells by Viral Aggregates Promotes
798 Early Viral Proliferation and Reveals a Cellular-Level Allee Effect. Curr Biol. 2018 Oct
799 22;28(20):3212-3219.e4.

800 41. Farrell A, Brooke C, Koelle K, Ke R. Coinfection of semi-infectious particles can contribute
801 substantially to influenza infection dynamics. bioRxiv [Internet]. 2019 Feb 12 [cited 2019
802 Jun 26]; Available from: http://biorxiv.org/lookup/doi/10.1101/547349

803 42. Koelle K, Farrell AP, Brooke CB, Ke R. Within-host infectious disease models
804 accommodating cellular coinfection, with an application to influenza. Virus Evol [Internet].
805 2019 Jul 1 [cited 2019 Jul 31];5(2). Available from:
806 https://academic.oup.com/ve/article/doi/10.1093/ve/vez018/5529690

807 43. Díaz-Muñoz SL, Sanjuán R, West S. Sociovirology: Conflict, Cooperation, and
808 Communication among Viruses. Cell Host Microbe. 2017 Oct;22(4):437–41.

809 44. Reed LJ, Muench H. A simple method of estimating fifty per cent endpoints. Am J
810 Epidemiol. 1938 May;27(3):493–7.

811 45. Matlin KS. Ammonium chloride slows transport of the influenza virus hemagglutinin but
812 does not cause mis-sorting in a polarized epithelial cell line. J Biol Chem. 1986 Nov
813 15;261(32):15172–8.

814 46. Hoffmann E, Stech J, Guan Y, Webster RG, Perez DR. Universal primer set for the full-
815 length amplification of all influenza A viruses. Arch Virol. 2001 Dec 1;146(12):2275–89.

816

817

818 **FIGURE LEGENDS**

819 **Fig. 1. Precise quantification of actual bulk MOI. (A)** Effect of 40 uM T705 treatment on
820 extracellular virus titers at 3 hpi and 6 hpi. MDCK cells were infected with PR8 at the indicated
821 MOIs in the absence (PBS; solid bars) or presence of T705 (checkered bars). TCID50 present in
822 supernatant was measured at 3 hpi and 6 hpi. **(B)** Quantification by RT-qPCR of virus present in
823 inoculum (0 hpi; "added MOI"), virus adsorbed to cells after 1 hpi (calculated by subtracting
824 extracellular virus present at 1hpi from that present in input at 0 hpi; "adsorbed MOI"), and virus
825 expected to actually contribute to infection (calculated by subtracting 1hpi and 3hpi GE amounts
826 from input 0 hpi amount; "actual MOI") for each of the indicated intended bulk MOI groups. Data
827 presented as viral genome equivalents (GE) per cell, with each point showing data from a single
828 infection well.
829
830 **Fig. 2. Cell death rates are time-dependent but virus input-independent. (A-D)** MDCK cells
831 were infected with PR8 at a range of intended bulk MOIs and the percentage of surviving cells
832 (compared with an uninfected control counted at time of inoculation) was determined at the
833 indicated times post-infection by trypan blue exclusion. Actual bulk MOIs were determined for
834 each replicate using the RT-qPCR method described in Fig. 1. Each data point shows the
835 percentage of surviving cells in a single infection well at its measured actual bulk MOI. Lines show
836 the statistical fits of the different cell death models to the experimental data. **(E)** Infected cell death
837 rates predicted by the time-dependent, input-independent model listed in Table 1.
838
839 **Fig. 3. Cellular co-infection increases the rate and efficiency of virus production. (A)** Virus
840 output from MDCK cells infected with PR8 over the indicated range of bulk MOIs. The total viral
841 output (GE/mL) from single cycle infections was measured by RT-qPCR at the indicated times
842 post-infection and plotted as a function of the bulk MOI for each infection well. Trend lines
843 represent linear regressions (log(GE/mL), log(MOI) scale) for each timepoint (6 hpi: slope (m) =
844 2.15, $R^2 = 0.87$, slope significantly non-zero: $p < 0.0001$; 12 hpi: slope (m) = 1.13, $R^2 = 0.69$, slope
845 significantly non-zero: $p = 0.0001$; 18 hpi slope (m) = 0.90, $R^2 = 0.76$, slope significantly non-zero:
846 $p < 0.0001$) plotted on the semilog scale. One-way ANOVA Tukey's multiple comparison of effects
847 of MOI on viral output at 6 hpi vs 12 hpi ($p = 0.0024$) or 18 hpi ($p = 0.0002$). **(B-D)** Different time-
848 dependent virus output models statistically fit to viral output data at the indicated timepoints. **(E)**
849 Model-predicted virus output dynamics. Predictions are shown for the best virus output model, as
850 determined by ΔAIC (the time-dependent, saturating input-dependent model). Dynamics for
851 various cellular input levels (i = 1, 4, 8) are shown as a function of time. **(F)** Viral replication
852 efficiency (calculated as the ratio of output viral genomes over mean input viral genomes) plotted
853 at each timepoint as a function of bulk MOI. Trend lines represent linear regressions (on the
854 log(replication efficiency), log(MOI) scale) for data from each timepoint, plotted on the semilog
855 scale. At 12 hpi and 18 hpi, the proportion of replication efficiency variance that was explained by
856 MOI was small ($R^2 = 0.08$ and $R^2 = 0.004$, respectively). At 6 hpi, the proportion of replication
857 efficiency variance that was explained by MOI was greater ($R^2 = 0.71$) and the correlation between
858 MOI and virus output was significantly positive ($p < 0.0001$). **(G)** 2.5×10^6 TCID50 of PR8 virions
859 were used to infect differing numbers of MDCK cells (6×10^5, 6×10^6, and 2×10^7), and viral output
860 per sample was quantified by TCID50 at 6 hpi. Data are presented as total output TCID50 per
861 sample.
862
863 **Fig. 4. Cellular co-infection enhances type III (but not type I) IFN induction.** A549 cells were
864 infected with PR8 under single cycle conditions at a range of bulk MOIs. Levels of cellular IFNB1
865 and IFNL1 transcript were measured by RT-qPCR at the indicated timepoints, compared to levels

in mock cells, and plotted relative to actual MOI for each infection well. **(A)** IFNB1 induction at 8 hpi and 18 hpi. Based on log-log linear regression, significance of a non-zero slope for normalized IFNB1 level vs. actual MOI: 8 hpi, $p = 0.78$; 18 hpi, $p = 0.0002$. **(B)** IFNL1 induction at 8 hpi and 18 hpi, trend lines represent log-log linear regression with positive correlation between normalized IFNL1 induction and actual MOI at both timepoints ($p < 0.0001$). **(C)** Fit of the most preferred IFN induction model to 8 hpi and 18 hpi timepoint data (saturating input-dependent; solid line) that has the rate of IFNL1 induction scale linearly with viral input during the 0-8 hpi epoch and independent of viral input during the 8-18 hpi epoch. **(D)** Model predictions for the rate of IFNL1 induction over 0-8 hpi and 8-18 hpi epochs shown at different viral input levels ($i = 1, 10, 20$).

Fig. 5. Cellular co-infection decreases the potential for superinfection. (A) MDCK cells were simultaneously coinfected with rH1N2 (at a constant MOI) and rH3N1 (at varying input MOIs shown on the x-axis) under single cycle conditions; SIE would not be expected to occur during simultaneous coinfection. Plot shows the percentages of all cells infected with rH1N2 (H1+; includes co-infected cells), all cells infected with rH3N1 (H3+; includes co-infected cells), and cells coinfected with both (H3+H1+), as determined by flow cytometry at 19 hpi. Solid lines indicate the two-susceptibility state null model fit to these data. **(B)** MDCK cells were infected with rH3N1 at the varying input MOIs shown on the x-axis under single cycle conditions. 6 hours later, cells were superinfected with rH1N2 at a constant input MOI under single cycle conditions. Plot shows the percentages of all cells infected with rH1N2 (H1+; includes co-infected cells), all cells infected with rH3N1 (H3+; includes co-infected cells), and cells coinfected with both (H3+H1+), as determined by flow cytometry at 19 hpi. Statistical fits of the input-independent and input-dependent models are shown. **(C)** Model prediction of susceptibility to superinfection (with 1 being completely susceptible) as a function of viral input.

SUPPLEMENTAL FIGURE LEGENDS

Fig. S1. Precise quantification of actual MOI. Quantification of virus present in inoculum (0 hpi), remaining unbound virus following adsorption (1 hpi), and cell-free virus present at 3 hpi for each of the indicated intended bulk MOIs. Data presented as viral genome equivalents (GE) per cell, with each point showing data from a single infection well.

Fig. S2. Fits of time-independent virus production models to virus output. Time-independent models are fit to output data at 6, 12, and 18 hpi. Parameter estimates for these models are shown in Table 1.

Fig. S3. Fits of model assuming that rH3N1 and rH1N2 particles are Poisson distributed across cells in the simultaneous coinfection experiment. Data are shown with dots. Curves show Poisson model predictions.

TABLE LEGENDS

Table 1. Death rate models and their fit to data. Rows show the three considered models. For each model, the table lists the functional form of the death rate that the model assumes (α), with t represents time since infection (hpi) and i represents cellular input. The table also lists model parameter estimates, the residual sum of squares (RSS) of the parameterized model, and calculated ΔAIC values. ΔAIC values are calculated by taking the difference between a given model and the model with the lowest AIC value, with AIC values of a model calculated using the

914 equation $2k + n \ln(RSS)$, where k is the number of estimated parameters and n is the number of
915 data points ($n = 60$).
916
917 **Table 2. Virus output models and their fit to data.** Rows show the three time-independent
918 models and the three time-dependent models considered. For each model, the table lists the
919 functional form for the virus production rate ν, with t representing time since infection (hpi) and i
920 representing cellular input. The table also lists model parameter estimates, the residual sum of
921 squares (RSS) of the parameterized model, and calculated ΔAIC values. For the calculations of
922 ΔAIC, the number of data points is $n = 40$.
923
924 **Table 3. Model descriptions of IFNL1 induction.** Rows show the three considered models in a
925 given epoch. For each model, the table lists the functional form for the IFN induction rate ϕ (relative
926 to mock-infected cells), with t representing time since infection (hpi) and i representing cellular
927 input, and a description of the model parameters.
928
929 **Table 4. IFNL1 induction models and their fit to data.** For each of the 9 possible model
930 combinations (3 models for the 0-8 hpi epoch x 3 models for the8-18 hpi epoch), the table shows
931 the model parameter estimates, the residual sum of squares (RSS) of the parameterized model,
932 and calculated ΔAIC values. For the calculations of ΔAIC, the number of data points is $n = 41$.
933
934 **Table 5. Superinfection exclusion models and their fit to data.** Rows show the two considered
935 models: an input-independent model and an input-dependent model. Each superinfection
936 exclusion model estimated the value of only a single parameter (s or r), with three additional
937 parameter values (rH1N2 input MOI, and fractions x and y) set based on the statistical fit of the
938 simultaneous coinfection model to the coinfection data (**Fig. 5A**; Methods). For each SIE model,
939 the table lists the functional form for cell susceptibility, with i representing cellular MOI. The table
940 also lists model parameter estimates, the residual sum of squares (RSS) of the parameterized
941 model, and calculated ΔAIC values. For the calculations of ΔAIC, the number of data points is n
942 $= 45$.